Switchable directional sound emission with improved field confinement based on topological insulators

Ailing Song,[1,2,a] (iD) Junfei Li,[2] (iD) Chen Shen,[2] (iD) Tianning Chen,[1,b] and Steven A. Cummer[2,c] (iD)

AFFILIATIONS

[1]School of Mechanical Engineering, Xi'an Jiaotong University, Xi'an, Shaanxi 710049, China
[2]Department of Electrical and Computer Engineering, Duke University, Durham, North Carolina 27708, USA

[a]Author to whom correspondence should be addressed: ailingsong@outlook.com
[b]tnchen@xjtu.edu.cn
[c]cummer@ee.duke.edu

ABSTRACT

Directional sound emission and reception are important in many practical applications, such as acoustic imaging, communications, and structural health monitoring. In this Letter, we propose and demonstrate an acoustic antenna for realizing switchable directional sound emission with improved field confinement. We construct the antennas with two rotatable phononic crystals to form different zigzag and armchair interfaces, then numerically and experimentally investigate their radiation performance. The simulated and measured sound pressure fields are in good agreement, which shows that the valley-projected edge states are excited with angular selectivity at the interfaces and then directionally radiate in different directions for different interfaces. In addition, the far-field radiation patterns of the proposed antennas clearly illustrate improved confinement of acoustic energy along the radiation directions, which can be attributed to the double C_3 symmetry of the snowflake-like scatterers employed to construct the antennas. Our proposed antenna greatly enriches the functionalities of topological insulators and provides a practical method to design acoustic devices with switchable and improved directional emission.

Published under license by AIP Publishing. https://doi.org/10.1063/5.0012290

In recent years, acoustic wave manipulation has attracted increasing attention due to its potential applications in many fields.[1,2] Acoustic metamaterials with extraordinary properties have served as one of the primary methods to manipulate acoustic waves, such as phononic crystals,[3,4] acoustic metasurfaces,[5,6] acoustic cloaking devices,[7,8] and more. Many functionalities including acoustic bandgaps,[9] wavefront modulation,[10,11] and asymmetric wave manipulation[12–14] have been achieved based on acoustic metamaterials. Directional sound emission and reception play a key role in numerous applications including acoustic imaging,[15] communications,[16] and structural health monitoring.[17] A directional acoustic antenna (DAA) is such a device that radiates or receives greater power in specific directions and has attracted considerable attention due to its extensive applications.[18]

With the rapid development of acoustic metamaterials, it has been recently demonstrated that enhanced directional sound emission or reception can be realized by phononic crystals,[19–21] Mie resonant structures,[22–24] anisotropic metamaterials,[25,26] and near-zero-index metamaterials.[27] However, these systems sometimes suffer from a

broad half-power beam width (HPBW) or unavoidable side lobes, and therefore, the acoustic waves cannot completely radiate in the target directions. Quan et al.[28,29] reported sound beam collimation through a plate with periodic Helmholtz resonators and slit structure, and Li et al.[5] designed a bianisotropic lossless metasurface to achieve scattering-free directional transmission. In addition, topological systems with advantages of high stability and efficiency offer great potential to overcome these barriers in DAAs. Nevertheless, the literature on topological insulator-based acoustic antennas has remained scarce, and Fleury et al.[30] theoretically proposed a topologically protected acoustic leaky-wave antenna. It was not until recently that two directional antennas based on topological transport of sound were introduced; Zhang et al.[31] and Xie et al.[32] demonstrated that directional radiation can be achieved at the interface between two phononic crystals. However, these two antennas have limited tunability of the radiation direction. There is still space to improve the transmission performance of topological insulator-based DAAs. As the tunability and directional sound confinement of DAAs are critical characteristics

for practical applications, it is necessary to explore new methods to overcome the current limitations and design DAAs with switchable and improved directional sound emission.

In this Letter, we propose a DAA composed of two rotatable phononic crystals to realize switchable directional sound emission with improved field confinement. The valley-projected edge states are excited with angular selectivity and then directionally radiate in different directions ($0°$, $+\theta$, and $-\theta$) for different zigzag and armchair interfaces. Theoretical analysis, numerical simulations, and experiments are carried out to investigate the radiation performance of DAAs. Our work focuses on analyzing the field confinement performance of the transmitted waves, which has been rarely reported in previous works on topological insulators.[33,34] It is found that the proposed antennas can better confine the energy to propagate along the radiation directions by introducing the interfaces and leveraging the edge states, which is a distinctive advantage over the antennas composed of other types of scatterers. In addition, the realization method of switchable emission directions by rotating the phononic crystals and forming different interfaces has been proved to be easy to operate and feasible in experiments. The proposed antenna greatly enriches the functionalities of topological insulators and allows the realization of switchable and improved directional emission.

The proposed antenna is constructed by two rotatable phononic crystals with different symmetry-broken scatterers, and the unit cells of two phononic crystals are fixed on two bottom plates with especially designed boundaries. By simply rotating each phononic crystal by $90°$, the DAAs with different zigzag and armchair interfaces can be obtained to achieve different sound emission directions represented by θ_t: $0°$, $+\theta$, and $-\theta$, as shown in Figs. 1(a)–1(c). The incident angle of acoustic waves illuminating in the antenna is α. Phononic crystals A′ and B′ are obtained by rotating A and B by $90°$ clockwise, respectively. The antenna is composed of snowflake-like scatterers[35] arranged in the triangular lattice with a lattice constant of $a = 5.4$ cm, as shown in Fig. 1(d). The snowflake-like scatterer has six legs, the leg width is
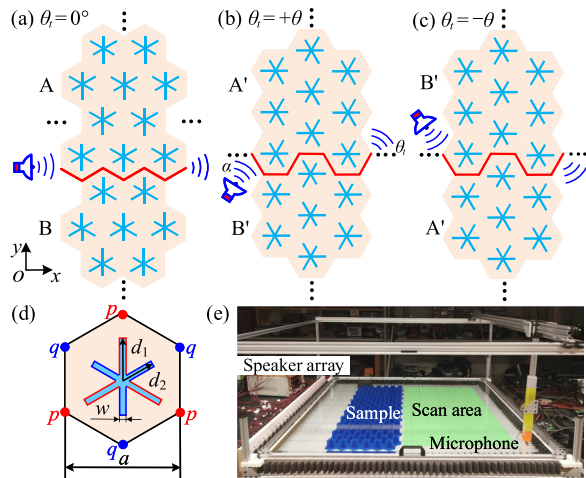
$w = 2$ mm, and the leg lengths are d_1 (red outlines) and d_2 (blue outlines). The mirror symmetry of the unit cell can be broken by changing the difference between d_1 and d_2 ($\Delta d = d_1 - d_2$) while keeping the mean length $d_m = (d_1 + d_2)/2 = 18$ mm constant when we vary Δd. In our design, the unit cells of phononic crystals A and A′ (B and B′) have $\Delta d = -4$ mm ($\Delta d = 4$ mm).

Breaking the mirror symmetry provides an opportunity to form interfaces, and the selective excitation of edges states at interfaces is the key point to realize directional emission. It is necessary to investigate the dispersion relations, the mode inversion, and valley Chern numbers of the unit cell to help the engineering of the edge states. The mirror symmetry breaking is achieved by perturbing the length of the legs according to $d_1 = d_m + \Delta d/2$ and $d_2 = d_m - \Delta d/2$. For $\Delta d = 0$, the C_{6v} point group symmetry (sixfold rotational symmetry and mirror symmetry) leads to Dirac degeneracy protected at K and K′ points, and so six single Dirac cones appear in the first Brillouin zone (BZ) in Fig. 2(a). When Δd is nonzero, the symmetry reduces from C_{6v} to C_3 (threefold rotational symmetry) due to the mirror symmetry breaking. This change lifts Dirac degeneracy to form an omnidirectional bandgap as shown in Fig. 2(b), which can be used to engineer the edge states and realize directional emission. Figure 2(c) shows that a Dirac cone occurs at 2941 Hz in the $\Delta d = 0$ case, while a complete bandgap ranging from 2726 Hz–3181 Hz occurs in the $\Delta d = 4$ mm case. The band evolution and the valley states are shown in Fig. 2(d). It is observed that the bandgap becomes wider with the increase in the absolute value of Δd. The valley states p^- and q^+ display typical vortex

FIG. 1. Acoustic antennas with (a) zigzag interface AB, (b) armchair interface A′B′, and (c) armchair interface B′A′ for realizing different sound emission directions. (d) Unit cell with a snowflake-like scatterer. p and q indicate two inequivalent triangular lattice centers with C_3 symmetry. (e) Experimental setup.
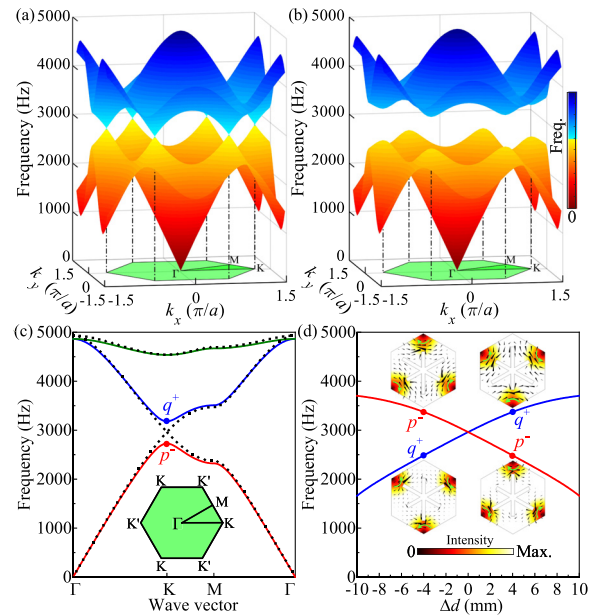

FIG. 2. Dispersion surfaces of the unit cell with (a) $\Delta d = 0$ and (b) $\Delta d = 4$ mm in the first BZ. (c) Band structures of the unit cell with $\Delta d = 0$ (black dots) and $\Delta d = 4$ mm (color lines) along the Γ-K-M-Γ direction. The inset shows the first BZ of the triangular lattice. (d) Evolution of band edge frequency as a function of Δd. The insets show the valley states located at the K point for $\Delta d = -4$ mm and $\Delta d = 4$ mm, where the jet color represents the amplitude of acoustic intensity, the arrows show the intensity direction, and the superscripts $+$ and $-$ represent the anticlockwise and clockwise vortex chirality, respectively.

features centered at p and q points, respectively. The valley states of the first two bands exhibit reversed vortex chirality when Δd crosses the critical point $\Delta d = 0$, which indicates the topological valley Hall phase transition caused by mirror symmetry breaking. The valley Chern number can be used to analyze the transport of edge states at interfaces and is defined as the integration of the Berry curvature over a small region around K(K') valley: $C_{K(K')} = \pm\mathrm{sgn}(\Delta_P)/2$, where Δ_P represents the geometrical perturbation strength and the sign of Δ_P is solely determined by the sign of Δd. We can determine the sign of Δ_P as $\mathrm{sgn}(\Delta_P) = \mathrm{sgn}(f(p^-) - f(q^+)) = -\mathrm{sgn}(\Delta d)$ by analyzing the frequency of valley states at K(K') points and the valley Hall phases shown in Fig. 2(d). In our research, $\Delta_P > 0$ ($\Delta_P < 0$) for the unit cell with $\Delta d < 0$ ($\Delta d > 0$), and so the valley Chern numbers of the first band are $C_{K(K')} = \pm 1/2$ for $\Delta d < 0$ and $C_{K(K')} = \mp 1/2$ for $\Delta d > 0$. See the supplementary material for the summary of valley Chern numbers in the first BZ. Therefore, for the interface separating two phononic crystals with different acoustic valley Hall phases, the absolute difference in the valley Chern number across the interface is $\left|\Delta C_{K(K')}\right| = 1$, which predicts that edge states would emerge in the bandgap and propagate along the interface.

The DAA with a zigzag interface for realizing 0° directional emission is studied first, which is constructed by phononic crystals A and B, as shown in Fig. 1(a). Figure 3(a) clearly shows an edge-state band located in the bulk bandgap. The edge state ϕ_{AB}^+ projected from the K valley moves forward, which can be predicted by the positive group velocity and the valley Chern number difference $\Delta C_K^{AB} = C_K^A - C_K^B = +1$. The K' valley projected edge state ϕ_{AB}^- propagates along the backward direction due to time-reversal symmetry. The α-dependent transmittance shown in Fig. 3(b) indicates that the edge state is excited

with angular selectivity and the maximum transmittance occurs at $\alpha = 0°$. As the forward moving edge state ϕ_{AB}^+ is projected from the K valley, the inset of Fig. 3(b) also illustrates the outgoing beam propagating along the $+x$ direction (purple arrow) based on the momentum conservation along the right sample boundary, where the green dashed line represents the sample boundary and the black dashed circle represents the equifrequency contour in free space. To confirm this, we numerically and experimentally investigate the transmitted field distributions when a Gaussian beam of 3000 Hz horizontally impinges on interface AB. The two-dimensional waveguide for the sound pressure field measurement with a 3D printed sample is shown in Fig. 1(e). See the supplementary material for the details of numerical simulations and the experimental setup. The incident Gaussian beam widths in experiments remain the same as those in simulations. The simulated sound pressure field in Fig. 3(c) clearly shows that the edge state is well excited and the transmitted wave propagates along the $+x$ direction as expected. The measured field agrees well with the simulated result. The far-field radiation pattern of the normalized energy density is calculated by performing spatial Fourier transform along a line in the near field, in which the evanescent waves are excluded and only propagating waves are included, and so it dictates the acoustic propagation performance in the far field. The radiation patterns for DAAs composed of different scatterers are shown in Fig. 3(d); it should be noted that all these scatterers have the same overall size. For snowflake-like scatterers, the side lobes are significantly suppressed, and the transmitted angles are $-0.18°$ (simulation) and $0.19°$ (experiment), in good agreement with theoretical predictions. Compared to other types of scatterers, the snowflake-like scatterer shows improved field confinement with the smallest half-power beam width (HPBW) and high beam efficiency (BE): the HPBWs are 11.93° (simulation) and 11.52° (experiment), and the BEs are 98.57% (simulation) and 99.53% (experiment). The improved field confinement is attributed to the double C_3 symmetry of snowflake-like scatterers [both three long legs with red outlines and three short legs with blue outlines in Fig. 1(d) have C_3 symmetry], which makes acoustic energy better confine to the target direction. Differently, the triangle,[36] three circle,[28] and three leg[37] scatterers only have single C_3 symmetry, which results in the attenuation of field confinement. Particularly, we can add three more legs in a three leg scatterer to obtain a snowflake-like scatterer; it is found that the field confinement performance of the antenna is significantly improved. See the supplementary material for detailed comparison.

Next, the DAAs with armchair interfaces for realizing $+\theta$ and $-\theta$ directional emission are studied. There are two different armchair interfaces depending on the position of phononic crystals A' and B' with respect to the interface: interface A'B' (A' on top and B' on bottom) shown in Fig. 1(b) and interface B'A' (B' on top and A' on bottom) shown in Fig. 1(c). Figure 4(a) shows the band structure of the superlattice containing interfaces A'B' and B'A'; it is observed that four edge-state bands fall within the bulk bandgap. The edge state $\phi_{A'B'}^+$ ($\phi_{B'A'}^+$) at interface A'B' (B'A') is projected from the K(K') valley and propagates along the $+\theta$ ($-\theta$) direction. Both edge states move forward, which can also be predicted by the positive group velocities and the valley Chern number difference $\Delta C_K^{A'B'} = C_K^{A'} - C_K^{B'} = +1$ and $\Delta C_{K'}^{B'A'} = C_{K'}^{B'} - C_{K'}^{A'} = +1$. Based on the conservation of momentum along the sample boundary (green dashed line) as shown in the inset of Fig. 4(b), the transmitted angle of the outgoing beam θ_t
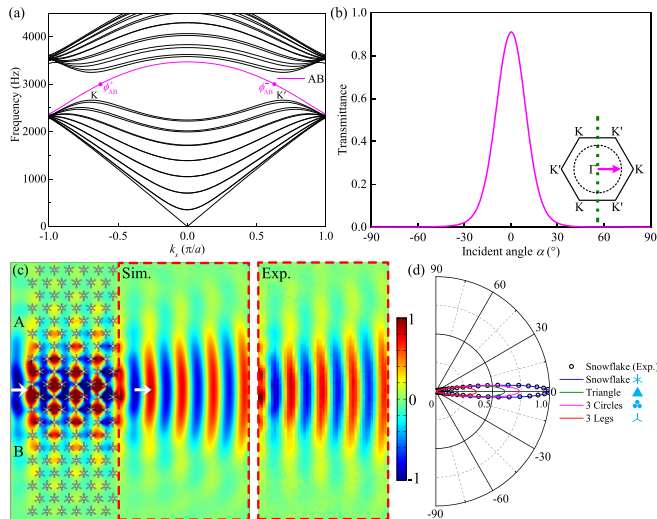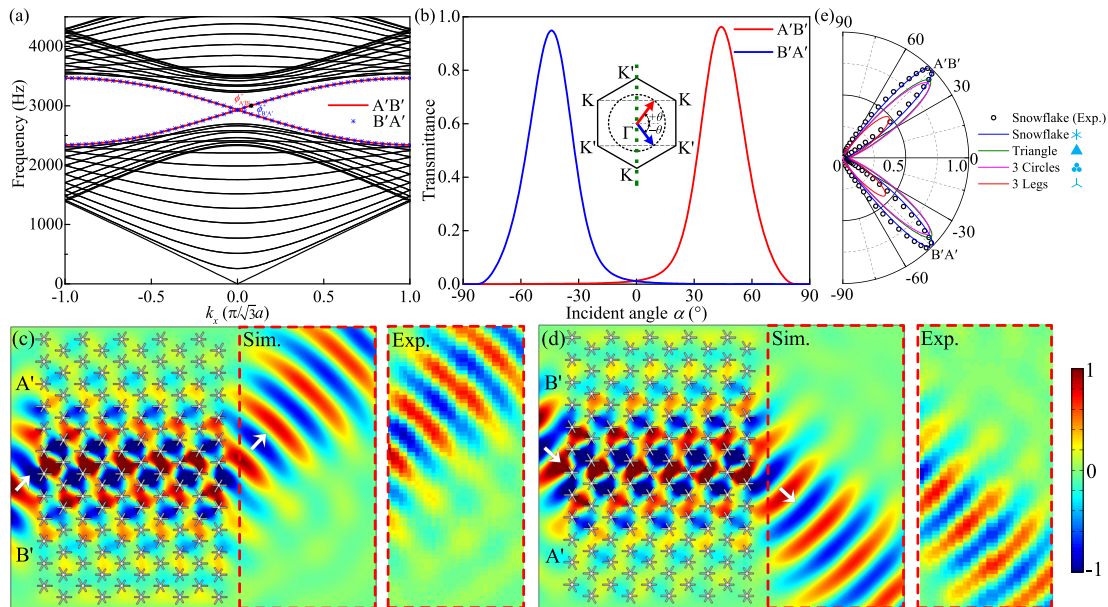

FIG. 3. (a) Band structure of the superlattice containing interface AB showing bulk bands (black lines) and the edge-state band (purple line). The superscripts $+$ and $-$ in ϕ_{AB}^+ and ϕ_{AB}^- represent the forward and backward moving edge states, respectively. (b) Transmittance of the DAA with interface AB as a function of incident angle α. The inset shows the **k**-space analysis on the outcoupling of the edge state at interface AB. (c) Simulated and measured sound pressure fields at 3000 Hz for interface AB with $\alpha = 0°$. (d) Far-field radiation patterns at 3000 Hz for DAAs with zigzag interfaces composed of different scatterers, where the lines and circles represent the simulated and measured results, respectively.

FIG. 4. (a) Band structure of the superlattice containing interfaces A′B′ (red lines) and B′A′ (blue snowflake symbols). (b) Transmittance of the DAA with interfaces A′B′ (red) or B′A′ (blue) as a function of the incident angle α. The inset shows the **k**-space analysis on the outcoupling of edge states at interfaces A′B′ and B′A′. Simulated and measured sound pressure fields when a Gaussian beam of 3000 Hz impinges on (c) interface A′B′ with $\alpha = +44.89°$ and (d) interface B′A′ with $\alpha = -44.89°$. (e) Far-field radiation patterns at 3000 Hz for DAAs with armchair interfaces composed of different scatterers, where the lines and circles represent the simulated and measured results, respectively.

satisfies: $k_b = k_0 \sin \theta_t$, where k_b is the projection of K or K′ points on the sample boundary, which can be expressed as $k_b = |\Gamma K| \sin 30° = 2\pi/3a$ or $k_b = |\Gamma K'| \sin(-30°) = -2\pi/3a$, and k_0 is the wave number in free space, $k_0 = 2\pi f/c$. The transmitted angle is predicted as $\theta_t = \pm \sin^{-1}(c/3af)$ for waves leaving interfaces A′B′ and B′A′. Based on the time reversal symmetry of the system, the valley-projected edge states can be well stimulated at the incident angle $\alpha = \pm \sin^{-1}(c/3af)$. In our design, the optimal transmittance occurs at $\alpha = +44.89°$ ($\alpha = -44.89°$) for interface A′B′ (interface B′A′). The α-dependent transmittance shown in Fig. 4(b) indicates that the edge states are angularly excited and the maximum transmittance occurs at $\alpha = +44°$ ($\alpha = -44°$) for interface A′B′ (interface B′A′), which is consistent with the **k**-space analysis. The acoustic propagation in DAAs with interfaces A′B′ and B′A′ is then numerically and experimentally investigated. The edge state is well excited at $\alpha = +44.89°$ and propagates along the $+\theta$ direction in Fig. 4(c), while the edge state is well excited at $\alpha = -44.89°$ and propagates along the $-\theta$ direction in Fig. 4(d). The far-field radiation patterns of DAAs with armchair interfaces A′B′ and B′A′ are shown in Fig. 4(e). For snowflake-like scatterers, the side lobes are significantly suppressed and the transmitted angles are 45.41° (simulation) and 44.94° (experiment) for interface A′B′ and are −44.86° (simulation) and −45.49° (experiment) for interface B′A′. The snowflake-like scatterer also shows improved field confinement compared to other types of scatterers, the HPBWs of snowflake-like scatterers are less than 18°, while those of other scatterers are more than 20°. See the supplementary material for detailed comparison. There are some small deviations between the simulated and measured results, which may be caused by the fabrication errors of the sample, the inevitable internal loss, and the imperfect boundaries.

In summary, we report theoretical analysis, numerical simulations, and experimental validation of a topological acoustic antenna capable of realizing switchable directional sound emission with improved field confinement along the radiation direction. The DAA contains two rotatable phononic crystals constructed by a snowflake-like scatterer, which undergoes phase transition during the mirror symmetry breaking process. By simply rotating each phononic crystal by 90°, different zigzag and armchair interfaces are formed in the DAAs to realize different radiation directions. The simulated and measured sound pressure fields are in good agreement, showing that the proposed antennas exhibit angularly selective excitation of edge states and directional emission at the interfaces. In addition, the proposed antennas exhibit improved field confinement with the smallest half-power beam width and high beam efficiency, which is attributed to the double C_3 symmetry of the snowflake-like scatterer. Our proposed antenna provides a practical method to manipulate sound with improved performance and has prospective applications in acoustic imaging, communications, and structural health monitoring.

See the supplementary material for the summary of valley Chern numbers, the details of numerical simulations and the experimental setup, the half-power beam width and beam efficiency of DAAs composed of different scatterers, and sound pressure fields at different incident Gaussian beam widths.

DATA AVAILABILITY

The data that support the findings of this study are available within this article and its supplementary material.

REFERENCES

[1]S. A. Cummer, J. Christensen, and A. Alù, Nat. Rev. Mater. **1**, 16001 (2016).

[2]B. Assouar, B. Liang, Y. Wu, Y. Li, J. C. Cheng, and Y. Jing, Nat. Rev. Mater. **3**, 460 (2018).

[3]Z. Y. Liu, X. X. Zhang, Y. W. Mao, Y. Y. Zhu, Z. Y. Yang, C. T. Chan, and P. Sheng, Science **289**, 1734 (2000).

[4]P. Wang, L. Lu, and K. Bertoldi, Phys. Rev. Lett. **115**, 104302 (2015).

[5]J. F. Li, C. Shen, A. Díaz-Rubio, S. A. Tretyakov, and S. A. Cummer, Nat. Commun. **9**, 1342 (2018).

[6]A. Díaz-Rubio, J. F. Li, C. Shen, S. A. Cummer, and S. A. Tretyakov, Sci. Adv. **5**, eaau7288 (2019).

[7]S. A. Cummer and D. Schurig, New J. Phys. **9**, 45 (2007).

[8]S. Zhang, C. G. Xia, and N. Fang, Phys. Rev. Lett. **106**, 024301 (2011).

[9]J. O. Vasseur, P. A. Deymier, B. Chenni, B. Djafari-Rouhani, L. Dobrzynski, and D. Prevost, Phys. Rev. Lett. **86**, 3012 (2001).

[10]Y. B. Xie, W. Q. Wang, H. Y. Chen, A. Konneker, B.-I. Popa, and S. A. Cummer, Nat. Commun. **5**, 5553 (2014).

[11]Y. Y. Zhu, J. Hu, X. D. Fan, J. Yang, B. Liang, X. F. Zhu, and J. C. Cheng, Nat. Commun. **9**, 1632 (2018).

[12]B. Liang, X. S. Guo, J. Tu, D. Zhang, and J. C. Cheng, Nat. Mater. **9**, 989 (2010).

[13]A. L. Song, J. F. Li, C. Shen, X. Y. Peng, X. H. Zhu, T. N. Chen, and S. A. Cummer, Appl. Phys. Lett. **114**, 121902 (2019).

[14]A. L. Song, J. F. Li, C. Shen, X. H. Zhu, T. N. Chen, and S. A. Cummer, Phys. Rev. Appl. **12**, 054048 (2019).

[15]T. X. Jiang, Q. B. He, and Z.-K. Peng, Phys. Rev. Appl. **11**, 034013 (2019).

[16]C. R. Berger, S. L. Zhou, J. C. Preisig, and P. Willett, IEEE Trans. Signal Process. **58**, 1708 (2010).

[17]S. B. Zhang, Q. B. He, H. B. Zhang, and K. Ouyang, IEEE Trans. Instrum. Meas. **66**, 671 (2017).

[18]C. A. Balanis, Antenna Theory Analysis and Design, 3rd ed. (Wiley, 2005).

[19]C. Y. Qiu and Z. Y. Liu, Appl. Phys. Lett. **89**, 063106 (2006).

[20]M. Z. Ke, Z. Y. Liu, P. Pang, C. Y. Qiu, D. G. Zhao, S. S. Peng, J. Shi, and W. J. Wen, Appl. Phys. Lett. **90**, 083509 (2007).

[21]T. X. Jiang, Q. B. He, and Z.-K. Peng, Appl. Phys. Lett. **112**, 261902 (2018).

[22]X. F. Zhu, B. Liang, W. W. Kan, Y. G. Peng, and J. C. Cheng, Phys. Rev. Appl. **5**, 054015 (2016).

[23]G. X. Lu, E. L. Ding, Y. Y. Wang, X. Y. Peng, J. Cui, X. Z. Liu, and X. J. Liu, Appl. Phys. Lett. **110**, 123507 (2017).

[24]J. J. Zhao, R. A. Jadhali, L. K. Zhang, and Y. Wu, Sci. Rep. **8**, 1018 (2018).

[25]J. Qian, H. X. Sun, S. Q. Yuan, and X. J. Liu, Appl. Phys. Lett. **114**, 013506 (2019).

[26]Y. Y. Chen, H. J. Liu, M. Reilly, H. Bae, and M. Yu, Nat. Commun. **5**, 5247 (2014).

[27]C. R. Ma, S. X. Gao, Y. Cheng, and X. J. Liu, Appl. Phys. Lett. **115**, 053501 (2019).

[28]L. Quan, X. Zhong, X. Z. Liu, X. F. Gong, and P. A. Johnson, Nat. Commun. **5**, 3188 (2014).

[29]L. Quan, F. Qian, X. Z. Liu, X. F. Gong, and P. A. Johnson, Phys. Rev. B **92**, 104105 (2015).

[30]R. Fleury, A. B. Khanikaev, and A. Alù, Nat. Commun. **7**, 11744 (2016).

[31]Z. W. Zhang, Y. Tian, Y. H. Wang, S. X. Gao, Y. Cheng, X. J. Liu, and J. Christensen, Adv. Mater. **30**, 1803229 (2018).

[32]B. Y. Xie, H. Liu, H. Cheng, Z. Y. Liu, S. Q. Chen, and J. G. Tian, Phys. Rev. Appl. **11**, 044086 (2019).

[33]X. J. Zhang, M. Xiao, Y. Cheng, M.-H. Lu, and J. Christensen, Commun. Phys. **1**, 97 (2018).

[34]G. C. Ma, M. Xiao, and C. T. Chan, Nat. Rev. Phys. **1**, 281 (2019).

[35]X. X. Wu, Y. Meng, J. X. Tian, Y. Z. Huang, H. Xiang, D. Z. Han, and W. J. Wen, Nat. Commun. **8**, 1304 (2017).

[36]J. Y. Lu, C. Y. Qiu, L. P. Ye, X. Y. Fan, M. Z. Ke, F. Zhang, and Z. Y. Liu, Nat. Phys. **13**, 369 (2017).

[37]Z. W. Zhang, Y. Tian, Y. Cheng, Q. Wei, X. J. Liu, and J. Christensen, Phys. Rev. Appl. **9**, 034032 (2018).